

## Full length article

# Lattice parameter misfit evolution during creep of a cobalt-based superalloy single crystal with cuboidal and rafted gamma-prime microstructures



James Coakley<sup>a, b, \*</sup>, Eric A. Lass<sup>c</sup>, Dong Ma<sup>d</sup>, Matthew Frost<sup>e</sup>, Howard J. Stone<sup>b</sup>, David N. Seidman<sup>a</sup>, David C. Dunand<sup>a</sup>

<sup>a</sup> Northwestern University, Department of Materials Science and Engineering, Evanston, IL 60208-3108, USA

<sup>b</sup> Department of Materials Science and Metallurgy, University of Cambridge, Cambridge CB3 0FS, UK

<sup>c</sup> Materials Science & Engineering Division, National Institute of Standards and Technology, Gaithersburg, MD 20899, USA

<sup>d</sup> Oak Ridge National Laboratory, Chemical and Engineering Materials Division, Neutron Sciences Directorate, Oak Ridge, TN 37831, USA

<sup>e</sup> Oak Ridge National Laboratory, Instrument and Source Division, Oak Ridge, TN 37831, USA

## ARTICLE INFO

## Article history:

Received 4 May 2017

Received in revised form

7 June 2017

Accepted 11 June 2017

Available online 13 June 2017

## Keywords:

Neutron diffraction

Superalloy

Creep

Misfit

Directional coarsening

## ABSTRACT

A [h00] oriented Co-based superalloy single crystal was crept under tension at 940 °C/100 MPa, resulting in a P-type raft morphology with extensive particle coalescence along the [h00] loading direction. However, particle coalescence was also observed in two perpendicular directions on the (h00) plane, normal to the loading axis. Tensile creep experiments were performed with *in-situ* neutron diffraction at 800 °C/500 MPa on this initially rafted  $\gamma'$  microstructure, and for comparison at (i) 900 °C/260 MPa, and at (ii) 750 °C/875 MPa, both with initially cuboidal  $\gamma'$  microstructures. The alloy was shown to exhibit a positive lattice parameter misfit, and during the first hour of creep at 900 °C/260 MPa, the lattice parameter evolution indicated changes in phase composition associated with  $\gamma'$  dissolution as the alloy achieved phase equilibrium at 900 °C. For all three *in-situ* creep measurements, there was a significant divergence of the  $\gamma'$  and  $\gamma$  lattice parameters as creep proceeded. The lattice parameter misfit values between the precipitates and the matrix approached their unconstrained values during creep, and were notably large compared to those of Ni-based superalloys. This is indicative of a loss of coherency at the precipitate/matrix interfaces. Such a loss of coherency at the precipitate/matrix interfaces will likely degrade certain mechanical properties such as fatigue resistance, as has been shown for the Ni-based superalloys.

© 2017 Acta Materialia Inc. Published by Elsevier Ltd. All rights reserved.

## 1. Introduction

Co-based superalloys that possess  $\gamma/\gamma'$  precipitate strengthened microstructures are the subject of extensive research and development as potential successors to the Ni-based superalloys that are currently used in the hot-sections of gas-turbine engines [1–20]. The Co-based superalloys developed thus far exhibit a positive lattice parameter misfit value (e.g. Refs. [17,20]), defined as  $\delta = 2[a_{\gamma'} - a_{\gamma}]/[a_{\gamma'} + a_{\gamma}]$  [21], where  $a_{\gamma'}$  and  $a_{\gamma}$  are the lattice parameters of the  $\gamma'$  precipitates and the  $\gamma$  matrix, respectively. This is in contrast to modern monocrystalline Ni-based superalloys

utilised for turbine blades, which typically possess a negative lattice parameter misfit value (e.g. Refs. [22,23]). Differences in lattice parameter misfit sign and magnitude are significant, as it is known that the lattice parameter misfit contributes to: (i) The precipitate morphology [24]; (ii) Alloy strengthening via coherency strains [25]; (iii) Precipitate coarsening rate and morphology evolution under elevated temperatures in the absence of an applied stress [24], and in the presence of an applied stress [26]; all of which contribute to the evolution of the microstructure and mechanical properties of the alloy. The relationship of lattice parameter misfit to deformation mechanisms in precipitate strengthened ferritic alloys has also been examined recently by *in-situ* neutron diffraction studies [27,28].

Rafting, also termed stress-coarsening, occurs in superalloys under creep conditions (*i.e.* under both elevated stresses and

\* Corresponding author. Northwestern University, Department of Materials Science and Engineering, Evanston, IL 60208-3108, USA.

E-mail address: [james.coakley@northwestern.edu](mailto:james.coakley@northwestern.edu) (J. Coakley).

temperatures), with the orientation of the rafts of aligned coalesced  $\gamma'$  particles being dependent on the direction of the applied stress and the lattice parameter misfit of the alloy [21]. Application of an external tensile stress along the nominal [h00] direction leads to differential levels of equivalent stress in the vertical (parallel to the applied stress) and horizontal (normal to the applied stress)  $\gamma$  matrix channels. For a negatively misfitting precipitate, the applied stress reduces the equivalent stresses in the vertical channels, and increases them in the horizontal, while the opposite is true for a positively misfitting precipitate. Dislocations penetrate the most highly stressed  $\gamma$  matrix channels and precipitate rafting at elevated temperatures and stresses initially occurs by  $\gamma'$  coalescence in the plane of the less highly stressed channels, where misfit/coherency stresses have not been relaxed by dislocations [29]. For a positive lattice parameter misfit alloy, it is expected that a rod-like  $\gamma'$  structure would be formed parallel to a tensile loading direction (P-type rafts), by  $\gamma'$  precipitate coalescence. It is also expected that a  $\gamma'$  plate-like structure would be formed normal to a compressive loading direction on the transverse face (N-type raft) [30]. This is phrased tentatively, as the authors are unaware of detailed three-dimensional microstructural studies that clearly illustrate the rafted precipitate morphologies in the Co-based superalloys. In contrast, the negative lattice parameter misfit Ni-based superalloys form  $\gamma'$  rods aligned parallel to the compressive loading direction (P-type raft), and a plate-like  $\gamma'$  structure normal to the tensile loading direction on the transverse face (N-type raft) [21,31].

Given the difference in lattice parameter misfit,  $\gamma'$  raft orientations and morphologies between Ni- and Co-based superalloy systems, studies relating lattice parameter misfit and rafting-type to mechanical properties of both Ni- and Co-based superalloys are of renewed interest. The present work correlates the evolution of  $\gamma$  and  $\gamma'$  lattice parameters measured *in-situ* during tensile creep of Co-based superalloy single crystals to their microstructural evolution. Samples with both cuboidal  $\gamma'$  and P-type rafted  $\gamma'$  starting microstructures have been studied. The results highlight that the large lattice parameter misfit value of current Co-based superalloys may be a design concern, as the  $\gamma'$  precipitates became less coherent with the  $\gamma$  matrix as the creep strain accumulated, presumably due to the formation of a network of interfacial dislocations. The results are compared to previously published *in-situ* neutron diffraction creep experiments of Ni-based superalloys with cuboidal  $\gamma'$  and initial N-type rafted  $\gamma'$  microstructures [23,32].

## 2. Experimental details

Nominally [h00] oriented bars of single crystal Co-based superalloy with composition Co-27.3Ni-2.7Al-1.4Ti-5.8W-4.2Mo-2.8Nb-2.8Ta wt.%, *i.e.* Co-28.8Ni-6.2Al-1.8Ti-2.0W-2.7Mo-1.8Nb-0.9Ta at.%, were cast by Alcoa-Howmet Research Center,<sup>1</sup> Michigan, U.S.A., and Exothermics Inc., New Jersey, U.S.A. The composition was determined by inductively coupled plasma optical emission spectrometry, and the alloy was labeled L19C. The bars were subjected to a homogenisation heat-treatment of 1300 °C/24 h, and aging at 900 °C/24 h followed by a 24 h furnace cool [20]. Secondary emission SEM images were recorded after electrolytically etching the  $\gamma$  phase with an aqueous solution of 2.5 vol.% phosphoric acid at 2.5 Vdc for  $\sim$  1 s.

Cylindrical tensile specimens with 6.35 mm gauge diameter and 40 mm gauge lengths were machined from the heat-treated bars.

*In-situ* neutron diffraction measurements were performed on VULCAN [33], the time-of-flight neutron engineering diffractometer at the spallation neutron source, Oak Ridge National Laboratory (ORNL), Tennessee, U.S.A. Samples were mounted such that the tensile stress was applied along the nominal [h00] direction of the bars. The irradiated length of each sample was 7 mm, centred at the middle of the specimen gauge length, and the experimental procedure was similar to that described previously elsewhere [20,23]. The loading axis was horizontal and the rig was positioned to give the longitudinal (h00) diffraction peaks in one detector and the transverse (0k0) diffraction peaks in the other.

*In-situ* neutron diffraction measurements were performed on two samples, with their as-aged cuboidal  $\gamma'$  microstructure, during creep at (i) 900 °C/260 MPa and (ii) 750 °C/875 MPa. A third sample was crept *ex-situ* at 940 °C/100 MPa for 20 h with  $\sim$  0.2% strain accumulation, with the aim of inducing a P-type rafted  $\gamma'$  microstructure. This sample was then measured with *in-situ* neutron diffraction during creep at (iii) 800 °C/500 MPa. All samples were crept under tension. The neutron beam frequency was 60 Hz in high-resolution mode and the diffracted beam was collected in the detectors continuously during the three *in-situ* creep tests. The data were subsequently chopped into 20 min segments to generate diffraction patterns as a function of creep time. Thermocouples were mounted along all samples, and the temperature difference across the 12 mm high-temperature extensometer mounted at the sample center was determined to be  $\sim$  5 °C. The thermal gradient across the central 7 mm irradiated length is lower than these bounds (as the irradiated length lies within the extensometer), and this length is therefore near isothermal [20,23].

## 3. Results

### 3.1. Results - microscopy

The microstructure following the initial heat-treatment is shown in Fig. 1a, and is representative of that seen in the two samples prior to *in-situ* diffraction measurements during creep at (i) 900 °C/260 MPa and at (ii) 750 °C/875 MPa. Fig. 1b and c shows the rafted  $\gamma'$  microstructure following *ex-situ* creep at 940 °C/100 MPa for 20 h with  $\sim$  0.2% strain accumulation, and is representative of the third sample prior to *in-situ* diffraction measurements during creep at (iii) 800 °C/500 MPa. Fig. 1b was imaged on the (0k0) plane, parallel to the tensile loading direction, while Fig. 1c was imaged on the (h00) plane, normal to the tensile loading direction. It is apparent that extensive precipitate coalescence has occurred parallel to the [h00] loading direction, Fig. 1b. However particle coalescence was also observed in two perpendicular directions on the (h00) plane, normal to the loading axis, Fig. 1c. Based on these SEM observations, it appears that the rafted  $\gamma'$  microstructure is rod-like, principally aligned along the loading direction, but with some rods also aligned in the two directions perpendicular to the loading direction.

### 3.2. Results - macroscopic creep curves

The macroscopic creep curves of the (i) 900 °C/260 MPa and (ii) 750 °C/875 MPa *in-situ* diffraction creep tests, both with an initial cuboidal  $\gamma'$  microstructures, are shown in Fig. 2, along with (iii) the 800 °C/500 MPa creep curve of the sample with an initially rafted  $\gamma'$  microstructure.

The 900 °C/260 MPa macroscopic creep data exhibited a somewhat classic creep curve with a creep incubation regime, followed by primary, secondary and tertiary creep regimes, Fig. 2 curve (i). The initial, short creep incubation period with zero strain accumulation over the first  $\sim$  30 min was followed by a

<sup>1</sup> Any mention of commercial companies or products herein is for information only; it does not imply recommendation or endorsement by NIST.

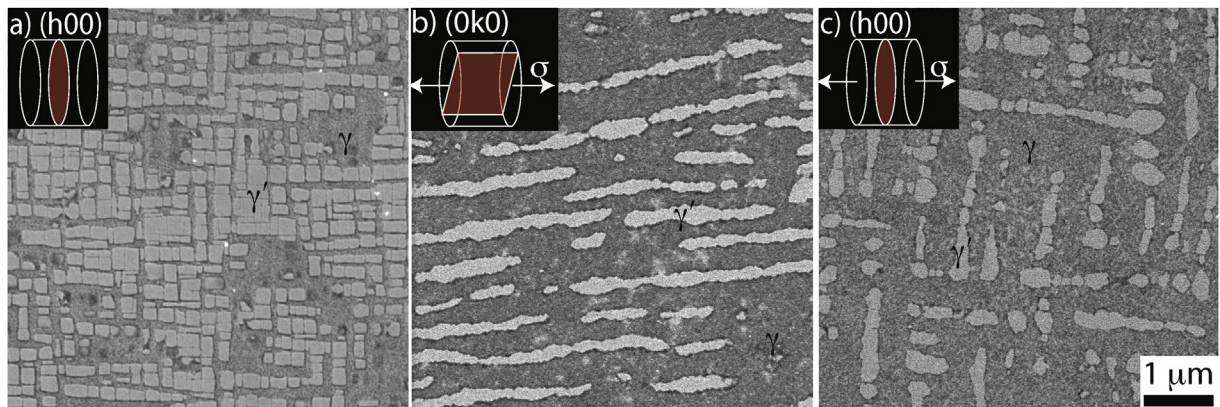


**Fig. 1.** Representative secondary emission SEM micrographs of etched cross-sections showing, at the same magnification, the microstructure of the single crystal Co-based superalloy (L19C): a) prior to creep testing with a cuboidal  $\gamma'$  microstructure imaged on the (h00) plane [20]; b) following tensile creep at 940 °C/100 MPa imaged on the (0k0) plane parallel to the loading direction; and c) imaged on the corresponding (h00) plane normal to the loading direction.

region of primary creep with 1.8% creep strain accumulated over 5 h. Between 5 - 10 h a region of quasi-steady-state creep was observed (where the average strain rate was  $8.79 \times 10^{-5} \pm 0.02 \times 10^{-5} \text{ s}^{-1}$ ), reaching a strain of 3.5%. The region of quasi-steady-state creep was followed by tertiary creep, where the creep rate increased with time. After 18.5 h total creep time, a total creep strain of  $\sim 16\%$  had accumulated. All creep experiments were halted prior to sample failure.

The 750 °C/875 MPa macroscopic creep data showed an initial burst of creep with 0.5% creep strain accumulated in the first 30 min, Fig. 2 curve (ii). A quasi-steady-state creep regime was again observed, with a higher strain rate of  $17.33 \times 10^{-5} \pm 0.01 \times 10^{-5} \text{ s}^{-1}$ , up to  $\sim 10$  h total creep time and a total of 6.5% overall strain accumulation. This regime was followed by a tertiary creep regime characterised by an increasing strain rate, with 13.5% total strain accumulation at the end of the 17 h creep test.

Finally, the 800 °C/500 MPa macroscopic creep data for the sample with an initially rafted  $\gamma'$  microstructure accumulated 1% creep strain in the first hour, followed by quasi-steady-state creep up to 17 h creep time (average strain rate:  $8.04 \times 10^{-5} \pm 0.01 \times 10^{-5} \text{ s}^{-1}$ ), reaching a strain of  $\sim 4.5\%$ , Fig. 2 curve (iii). This was followed by a region of tertiary creep with an increasing strain rate, reaching a final strain of 14% at the end of the 30 h creep test.

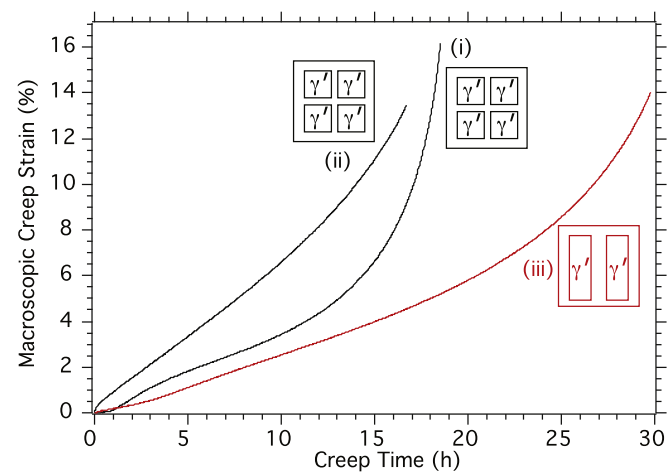


**Fig. 2.** Macroscopic creep curves of single crystal Co-based superalloy (L19C) crept at (i) 900 °C/260 MPa, and (ii) 750 °C/875 MPa (both with initial cuboidal  $\gamma'$  microstructures); and (iii) 800 °C/500 MPa (with initial rafted  $\gamma'$  microstructure).

### 3.3. Results - diffraction data

Diffraction data acquired in the vicinity of the {200} reflections at the beginning and end of each creep test are presented in Fig. 3. These data were integrated across the full detector banks. Both  $\gamma$  and  $\gamma'$  contribute to the {200} reflections, producing overlapping {200} peaks. The {300}  $\gamma'$  superlattice reflection (not shown) was of very low intensity, but was sufficient to unambiguously determine its inter planar spacing, which allowed the location of the {200}  $\gamma'$  peak to be determined from  $d_{\{200\}}' = (3/2) \times d_{\{300\}}'$ . The absence of strong {100} or {300}  $\gamma'$  superlattice single peak reflections inherently complicated the diffraction data analyses compared to previously published *in-situ* neutron diffraction studies of Ni-based superalloys [23,32]. Initially, for the cuboidal  $\gamma'$  microstructure crept at 900 °C/260 MPa, there was a third low intensity peak at the low d-spacing tail (1.798 Å) of the multicomponent peak, Fig. 3a and b. This low intensity peak quickly diminished during the creep test, and may have been a scattering contribution from the low volume fraction, fine scale, tertiary  $\gamma'$  particles present in the  $\gamma$  matrix. These fine-scale tertiary precipitates would have formed on furnace cooling from the prior 900 °C aging heat-treatment. They would be expected to quickly dissolve at the 900 °C creep temperature as the new elevated temperature phase equilibria was achieved, and would also be quickly consumed during coarsening at this temperature.

There was a clear separation of the  $\gamma$  and  $\gamma'$  peaks as creep proceeded at 900 °C/260 MPa, Fig. 3a and b. It was deemed satisfactory to fit these {200} data with a two peak fitting routine to account for reflections from (i) the  $\gamma$  matrix and (ii) the high volume fraction of larger secondary  $\gamma'$  particles. If the low volume fraction of fine ternary  $\gamma'$  precipitates was present during high-temperature diffraction measurements, and if these particles possessed a different constrained lattice parameter to the larger precipitates, this methodology accepted the error that a low intensity reflection to the {200} peak profile from the fine precipitates would be blurred into a two peak  $\gamma$  and  $\gamma'$  fitting routine.

The initial peaks of the cuboidal  $\gamma'$  microstructure at 750 °C/875 MPa, Fig. 3c and d, were notably different to those observed during creep testing at 900 °C/260 MPa, Fig. 3a and b. Clearly the rapid creep strain accumulation in the first 20 min of creep at this high stress (Fig. 2 curve (ii)) was altering the microstructure in this time frame, and the diffraction pattern presented was an averaged measurement during this 20 min window of rapid strain accumulation. Again the peak separation was clear during the creep test, and the {200} diffraction data was well fitted by a

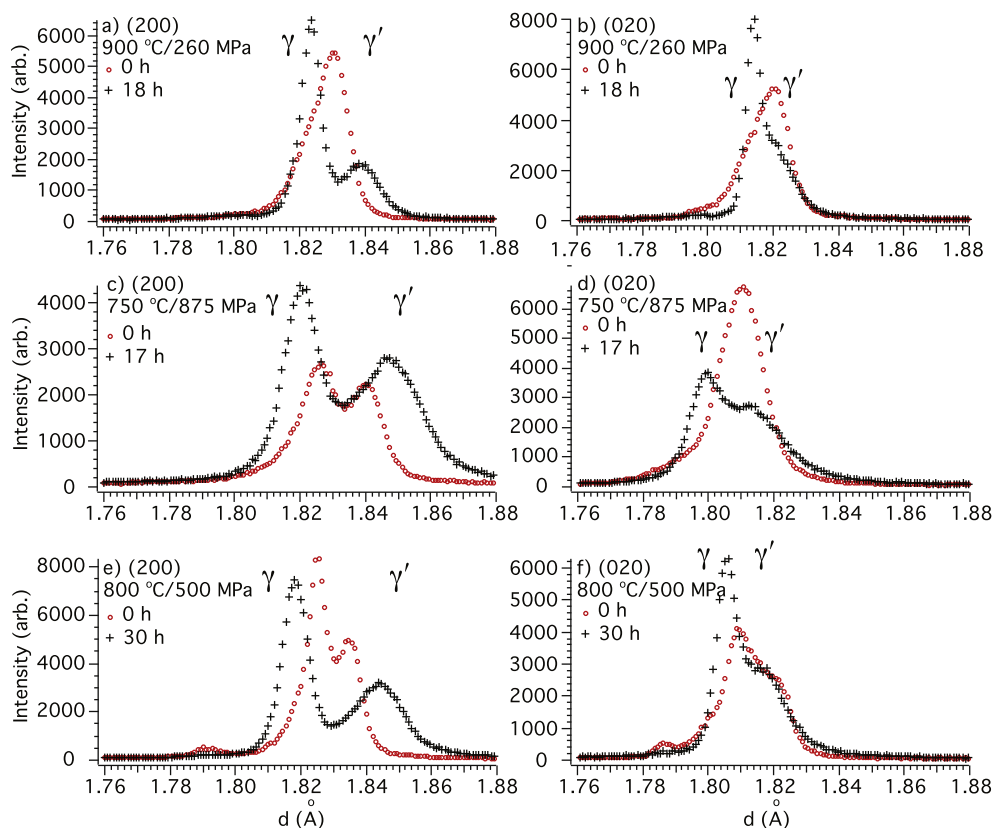


**Fig. 3.** In-situ diffraction patterns illustrating  $\gamma$  and  $\gamma'$  peak evolution measured under creep conditions at the beginning (red markers) and end (black markers) of each creep test at a, b) 900 °C/260 MPa for a sample with an initially cuboidal  $\gamma'$  microstructure, c, d) 750 °C/875 MPa for a sample with an initially cuboidal  $\gamma'$  microstructure, and e, f) 800 °C/500 MPa for a sample with an initially rafted  $\gamma'$  microstructure. Spectra are for a, c, e) (200) and b, d, e) (020) planes. (For interpretation of the references to colour in this figure legend, the reader is referred to the web version of this article.)

two peak fitting function. During this creep test, an increase in intensity of the (200) peaks was noted, and a decrease in the (020) peaks. It was unclear to the authors how this effect arose, and it was not investigated further as the focus of the current work was on lattice parameter evolution determined from peak positions.

Finally, the  $\gamma + \gamma'$  peaks were clearly separated in the (200) during creep at 800 °C/500 MPa of the pre-rafted  $\gamma'$  microstructure. A separate low intensity peak at lower d-spacing (1.791 Å) was also apparent in the initial measurement at the onset of creep, Fig. 3e. No other additional peaks were present elsewhere in the diffraction pattern that would indicate the presence of a third phase. As the low intensity peak disappeared during the creep test, it may be a contribution from fine  $\gamma'$  precipitates that dissolved, as discussed earlier. Whereas the (200) peaks were quite clearly separated, the (020) peaks were heavily overlaid, Fig. 3f, making it difficult to isolate with confidence the changes in peak broadening, peak position and peak intensities of each phase, all of which evolve during creep. As previously mentioned, it was not possible to implement constraints to the {200}  $\gamma'$  peak position based on an accurate fit from {300} or {100}  $\gamma'$  superlattice reflections, which may have allowed for the (020)  $\gamma$  and  $\gamma'$  peak positions to have been fitted with confidence during the 800 °C/500 MPa creep measurements. Therefore, this work presents the analysis of the longitudinal diffraction data alone, and omits the transverse data, which is not uncommon in the literature [34].

Two pseudo-Voigt functions were fitted to the (200)  $\gamma + \gamma'$  diffraction peaks by an iterative least-squares error minimisation procedure, in a similar manner to Refs. [20,23]. In the present study, it was found that the peak fitting routine converged to unique

solutions for the (200) diffraction data without constraining fitting parameters, as the peaks generally were sufficiently separated. A peak fit to the *in-situ* diffraction data is shown in Fig. 4.

The evolution of the (200)  $\gamma$  and  $\gamma'$  d-spacing is shown in Fig. 5, during creep at 900 °C/260 MPa (Fig. 5i), at 750 °C/875 MPa (Fig. 5ii) for samples with an initial cuboidal  $\gamma'$  microstructure, and at 800 °C/500 MPa for a sample with an initially rafted  $\gamma'$  microstructure (Fig. 5iii). The (200) d-spacing evolution of each phase is replotted in terms of elastic lattice strain changes  $(d_x - d_{x,0})/d_{x,0}$  that occur in each phase during creep, where  $d_x$  is the (200) d-

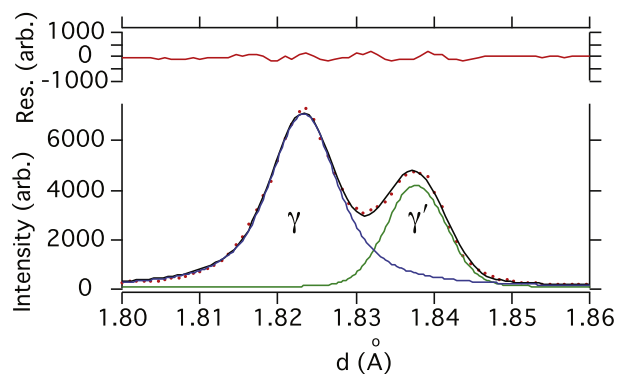


**Fig. 4.** A pseudo-Voigt doublet fit and residual error to the (200)  $\gamma + \gamma'$  peaks of experimental data measured between 100 – 120 min of creep at 800 °C/500 MPa with an initial rafted  $\gamma'$  microstructure.

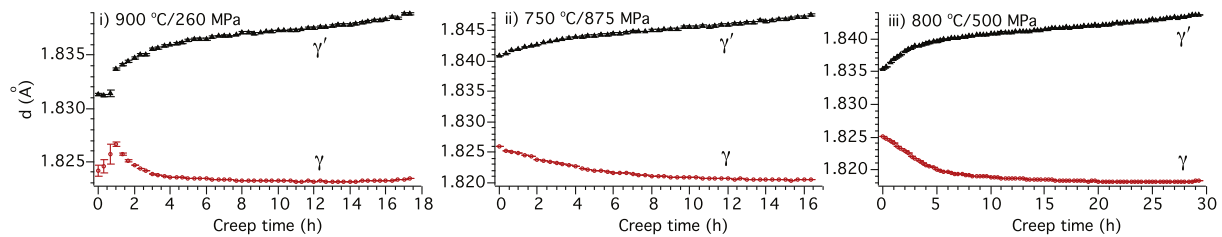


**Fig. 5.** Temporal evolution of the (200)  $\gamma$  and  $\gamma'$  d-spacing during tensile creep at i) 900 °C/260 MPa, ii) 750 °C/875 MPa, and iii) 800 °C/500 MPa. i, ii) Samples exhibited an initially cuboidal  $\gamma'$  microstructure, and iii) an initially rafted  $\gamma'$  microstructure. The error bars represent the uncertainty associated with the peak positions in the peak fits.

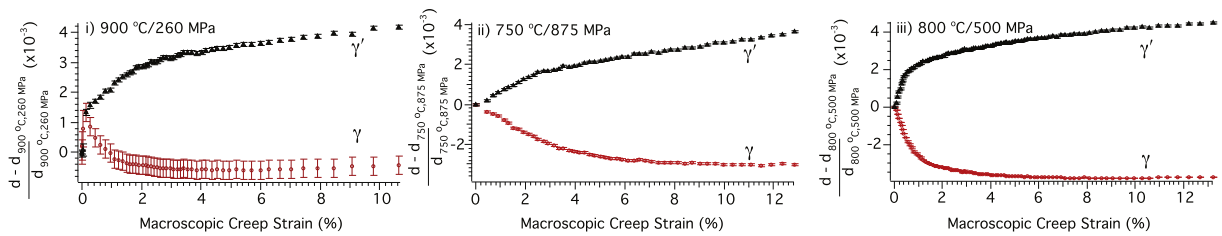


**Fig. 6.** Evolution of the (h00)  $\gamma$  and  $\gamma'$  lattice strains with respect to macroscopic creep strain during tensile creep at i) 900 °C/260 MPa, ii) 750 °C/875 MPa, and iii) 800 °C/500 MPa. i, ii) Samples exhibited an initially cuboidal  $\gamma'$  microstructure, and iii) an initially rafted  $\gamma'$  microstructure. The error bars represent the uncertainty associated with the peak positions in the peak fits.

spacing of phase  $x$  (i.e.  $\gamma$  or  $\gamma'$ ) during the creep test and  $d_{x,0}$  is the (200) d-spacing of each phase at the start of each creep test following heating and loading of each sample, Fig. 6. The lattice strain graphs are plotted against macroscopic creep strain. Finally, the data are replotted in terms of constrained lattice parameter misfit  $\delta$  against macroscopic creep strain, Fig. 7.

## 4. Discussion

### 4.1. Discussion - microscopy

The mean precipitate width of the secondary  $\gamma'$  particles of the cuboidal microstructure (Fig. 1a) was  $\bar{w} = 165 \pm 50$  nm, with the standard deviation calculated from traced areas using square-equivalence ( $\bar{w} = \overline{\text{area}}^{1/2}$ ). The area fraction was  $\sim 50 \pm 5\%$ , calculated from a representative cross-section of the alloy by pixel-counting image analysis.

Following creep at 940 °C/100 MPa for 20 h, the particle coalescence was dramatic in the [h00] direction parallel to the applied load (Fig. 1). However, particle coalescence was also noted along the

[0k0] and [00l] directions [36], mutually perpendicular to the applied stress (Fig. 1c). A plate-like morphology of  $\gamma'$  particles was not observed on either the (0k0) or (h00) planes (Fig. 1b and c) and the  $\gamma'$  raft morphology was rod-like, aligned and coalesced in the  $< 100 >$  directions. Pollock and Argon [29] speculated that the morphology of P-type  $\gamma'$  rafts tended towards corrugated plates in a positive lattice parameter Ni-based superalloy crept under tension. Thus, our observations indicate that P-type raft morphology may not necessarily be as simple as rods coalesced exclusively in the direction parallel to the tensile load, in positive lattice parameter misfit alloys.

The difference between the  $\gamma'$  precipitate volume fraction in the (0k0) and (h00) (following creep at 940 °C/100 MPa for 20h) fell within the range of error, and was  $\sim 23 \pm 3\%$  excluding the tertiary  $\gamma'$  particles. The range of particle sizes were also similar, the particles were up to  $\sim 2 - 5$   $\mu\text{m}$  in length with raft widths  $\sim 150 - 300$  nm in both planes. However, the average particle size of rafted precipitates in the (0k0) was approximately twice the average particle size in the (00l), and the particle number density per unit area in the (0k0) was approximately half that of the (00l). Thus it is clear that the extent of particle coalescence in the loading direction was greater than that in the perpendicular directions. The factor of two decrease in secondary  $\gamma'$  area fraction, as compared to the cuboidal microstructure (23 vs. 50%), is presumably related to the different cooling rates. The cuboidal  $\gamma'$  microstructure was furnace cooled over 24 h, while the rafted  $\gamma'$  microstructure was air-cooled to room temperature over a time scale of minutes.

According to Matan et al. [26], a loss of coherency in specific  $\gamma$  channels with an accompanying reduction in elastic misfit strain provides the driving force for rapid microstructural rafting to occur [26]. Thus, the raft morphology observed herein may be interpreted in light of Pollock and Argon [29], and Matan et al. Under tensile load, plastic deformation of the more highly deformed  $\gamma$  channels aligned parallel to the load occurred, and particles coalesced in the less highly strained channels aligned perpendicular to the applied load (which would form a rod-like structure parallel to the load). However, particle coalescence has clearly also occurred perpendicular to the load. Thus, plastic deformation of the less highly strained  $\gamma$  channels aligned perpendicular to the load may also

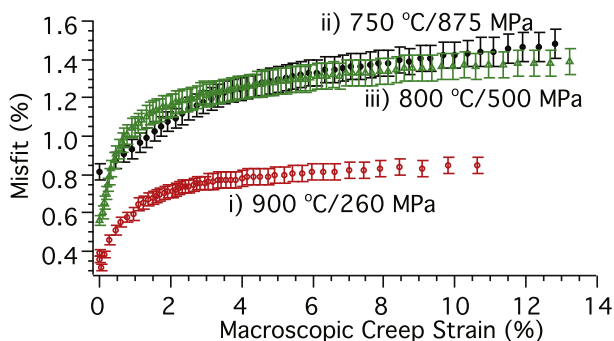


**Fig. 7.** Evolution of the (h00) lattice parameter misfit with respect to macroscopic creep strain during creep at i) 900 °C/260 MPa, ii) 750 °C/875 MPa, and iii) 800 °C/500 MPa. i, ii) Samples exhibited an initially cuboidal  $\gamma'$  microstructure, and iii) an initially rafted  $\gamma'$  microstructure. Error bars of 5% are presented.

have occurred, and particles coalesced in the more highly stressed channels. This contribution to the raft morphology could not be dominant, otherwise an N-type plate-like morphology would be observed.

4.2. Discussion - diffraction

The understanding of creep is inherently complicated due to the numerous microstructural parameters and deformation mechanisms that evolve with stress, temperature and time. Fig. 8 is a schematic representation of how certain creep-induced phenomena would be observed in a positive lattice parameter misfit superalloy when measuring the (h00)  $\gamma$  and  $\gamma'$  phase lattice parameters *in-situ* by neutron or X-ray diffraction. A similar schematic and explanation was first presented by the authors for a Ni-based superalloy single crystal with negative lattice parameter misfit [23]. The schematic and brief explanation below of the schematic have been altered for the case of a Co-based superalloy single crystal with positive lattice parameter misfit to aid the interpretation of the measured evolution of the  $\gamma$  and  $\gamma'$  lattice parameters.

From Fig. 8a, it is clear that correlating lattice parameter evolution during creep to a single microstructural change is difficult, as various microstructural changes exhibit similar signatures in the (h00) lattice parameter evolution. A loss of coherency of the  $\gamma'$  phase within the  $\gamma$  matrix would be observed as an increase in the (h00)  $\gamma'$  lattice parameter and a decrease in the  $\gamma$  lattice parameter, Fig. 8a. This occurs as atomic registry across the interface plane is lost, and the  $\gamma'$  lattice parameter approaches its equilibrium unconstrained value [23]. Similarly, the  $\gamma$  lattice parameter will decrease towards its equilibrium value as a result of the loss of constraint by the  $\gamma'$  phase.

A significant repartitioning of elements during creep would also

be observed by changes in the diffraction profiles [23], with the schematic example illustrating partitioning of elements with small atomic radii from the  $\gamma'$  to the  $\gamma$  and assuming precipitate volume fraction is constant, Fig. 8a. This would be observed as an increase of the  $\gamma'$  lattice parameter and a decrease of the  $\gamma$  lattice parameter, Fig. 8a. In the alloy studied, the lattice parameter misfit was essentially constant from room-temperature to 900 °C [20], thus a change in lattice parameter associated with element repartitioning was not observed. Pyczak et al. [17] noted a decrease in Co-9Al-9W at.% lattice parameter misfit above ~ 600 °C and hypothesized that this may be associated with a re-distribution of elements between precipitates and matrix.

If load transfer occurs to the  $\gamma'$  phase under yielding of the  $\gamma$  phase, this would be observed as an increase in the  $\gamma'$  lattice parameter and a decrease in the  $\gamma$  lattice parameter in the (h00) [23], Fig. 8a. Work hardening of an individual phase in a two-phase alloy may also be apparent in the diffraction data. In this case work hardening of the  $\gamma'$  phase would result in a higher load-bearing capacity of this phase and thus additional load transfer occurs, highlighted as an increase of the  $\gamma'$  lattice parameter and a decrease of the  $\gamma$  lattice parameter in the (h00). Similarly, work hardening of the  $\gamma$  phase alone would be observed as an increase in the  $\gamma$  lattice parameter and a decrease of the  $\gamma'$  lattice parameter in the (h00) [23].

As discussed elsewhere [23], on rapidly heating to the creep temperature, the alloy is likely to be in a non-equilibrium state, and equilibrium is subsequently achieved according to the lever rule, by (i) dissolution of  $\gamma'$  and (ii) shifting of phase compositions towards equilibrium at the creep temperature. Considering first the effect of precipitate dissolution on the stress distribution between the two phases, as the constrained elastic moduli of the  $\gamma$  ( $E_\gamma$ ) and the  $\gamma'$  ( $E_{\gamma'}$ ) phases are approximately equal [20], a stress redistribution will not occur between the precipitate and matrix due to a change

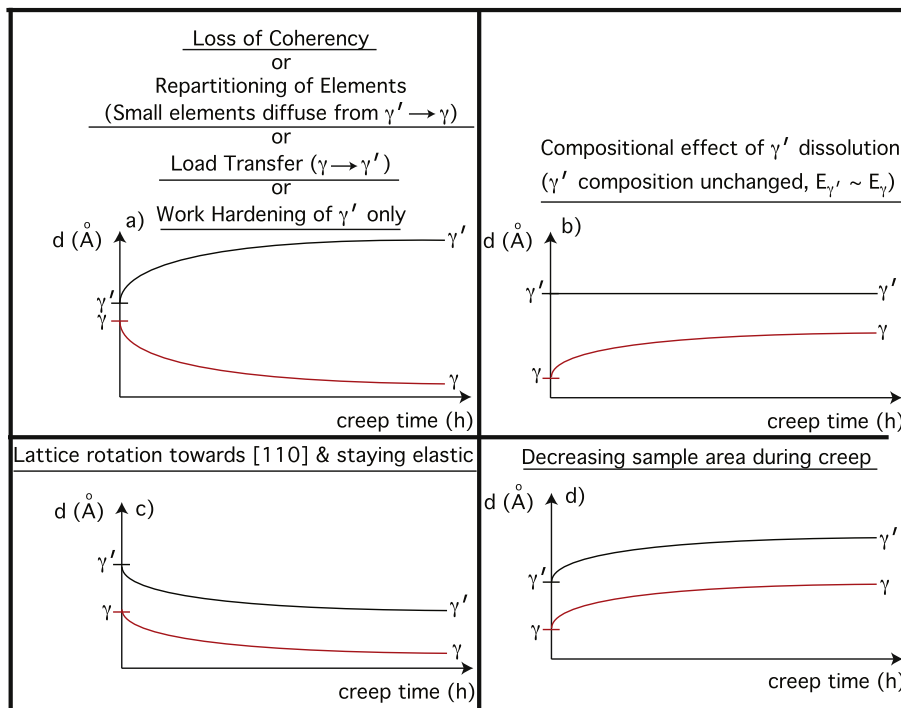


Fig. 8. Schematic plot of the (h00) lattice spacing evolution of the  $\gamma$  and  $\gamma'$  phases during tensile creep along the nominal [h00] direction for a positive lattice parameter misfit alloy that would be observed as a result of various microstructural evolutions that may occur during creep, specifically: a) If the  $\gamma'$  particles lose coherency with the  $\gamma$  matrix, or if there is diffusion of elements with small atomic radii from  $\gamma'$  to  $\gamma$  under constant precipitate volume fraction, or if the  $\gamma$  matrix yields and load is transferred to the  $\gamma'$  phase, or if work hardening of the  $\gamma'$  phase alone occurs; b) If dissolution of  $\gamma'$  occurs during creep conditions, with no change in the  $\gamma'$  composition and both phases possessing similar elastic moduli; c) If there is lattice rotation towards the stiffer [110] direction of both phases; d) If the sample area decreases during creep. Figure adapted from Ref. [23].

in the precipitate volume fraction [23]. Now considering the change in phase compositions towards equilibrium in the Ni–Al binary phase diagram [37,38], the  $\gamma/\gamma + \gamma'$  phase boundary has a relatively shallow slope against temperature compared to the  $\gamma + \gamma'/\gamma'$  phase boundary, which is near vertical. For a vertical  $\gamma + \gamma'/\gamma'$  phase boundary, the  $\gamma'$  equilibrium composition will be approximately constant with temperature, and only a change in the  $\gamma$  composition will occur, together with a change in phase volume fraction [23]. Therefore, for a positive lattice parameter misfit alloy, this shift towards phase equilibria at temperature would result in the dissolution of some of the  $\gamma'$  phase, releasing larger atomic radius solute atoms that must then be incorporated into the  $\gamma$  matrix. This would increase the  $\gamma$  lattice parameter, whilst the  $\gamma'$  lattice parameter would remain unchanged, Fig. 8b. If the phase boundaries of  $\gamma + \gamma'$  are similar for the Co-based superalloys as for Ni–Al, a large shift in the  $\gamma$  lattice parameter accompanied by little change in the  $\gamma'$  lattice parameter may be expected during  $\gamma'$  dissolution.

During creep of a superalloy single crystal, the tensile axis rotates towards the slip direction. Given that the [h00] direction is the least stiff direction in both Co- and Ni-based superalloys [16,35,39], the rotation will be towards a stiffer direction and would be observed as a decrease of lattice parameter value in both phases in the (h00) during creep at a constant stress  $\sigma$ , as  $\sigma = \epsilon E$ , Fig. 8c. Finally, a decrease in sample area, i.e. an increase in true stress, would be observed as an increase of lattice parameter value in both phases in the (h00) during creep [23], Fig. 8d.

Over the first hour of creep at 900 °C/260 MPa of the sample with an initially cuboidal  $\gamma'$  microstructure, the (200)  $\gamma'$  lattice parameter was quite constant, while that of the  $\gamma$  increased, Fig. 5i. This corresponded to an initial creep incubation period and onset of primary creep (Fig. 2, creep curve (i)). As previously discussed in this paper, this was likely to be associated with compositional effects indicative of  $\gamma'$  dissolution as the alloy achieved phase equilibrium at 900 °C, Fig. 8b. This interpretation is supported by the lower volume fraction of rafted  $\gamma'$  observed in SEM micrographs following creep at 940 °C (Fig. 1b and c). The comparison and agreement with previous diffraction measurements is noteworthy: over the first 2 h of creep at 1150 °C/100 MPa of the Ni-based superalloy CMSX-4 (with negative lattice parameter misfit), the  $\gamma'$  lattice parameter also remained close to constant, while that of the  $\gamma$  decreased towards the  $\gamma'$  value [23]. For a negative lattice parameter misfit alloy, this is the signature of compositional effects indicative of  $\gamma'$  dissolution.

Following this initial d-spacing evolution associated with compositional effects and precipitate dissolution, the (200)  $\gamma'$  d-spacing rapidly increased and that of the  $\gamma$  decreased during creep at 900 °C/260 MPa, as shown in Fig. 5i, and also plotted in terms of phase lattice strains against macroscopic creep strain in Fig. 6i. The same general trend of an increasing (200)  $\gamma'$  d-spacing and decreasing  $\gamma$  d-spacing was observed for all three *in-situ* diffraction creep tests, Figs. 5i–iii and 6i–iii. Referring to the (h00) lattice parameter misfit evolution during creep, Fig. 7, it was clear that large values of misfit were accumulating during the creep process, reaching ~0.85%, 1.5%, and 1.4% towards the end of the 900 °C/260 MPa, 750 °C/875 MPa, and 800 °C/500 MPa creep tests respectively. For comparison, the maximum magnitude of lattice parameter misfit measured during creep of the Ni-based superalloy CMSX-4 (with negative lattice parameter misfit) for cuboidal and rafted  $\gamma'$  microstructures was ~0.6%, and were typically lower than this maximum recorded, over numerous different creep conditions studied (650 °C/825 MPa, 715 MPa, 900 °C/460 MPa, and 1150 °C/100 MPa) [23,32].

Referring to Fig. 8, it is apparent that all three *in-situ* creep tests (Figs. 5i–iii and 6i–iii) were being dominated by a mechanism highlighted in Fig. 8a. It is unlikely that the  $\gamma'$  phase alone was

work-hardening, or that such extensive load transfer was occurring between precipitate and matrix, or that such extensive element repartitioning would occur at 750 °C/825 MPa. However, it is reasonable to interpret the lattice parameter evolution in terms of a loss of coherency at the (h00)  $\gamma/\gamma'$  interfaces by the development of dislocation networks. The loss of  $\gamma/\gamma'$  coherency by dislocations during creep is supported by TEM of Ni-based superalloys, for example [26], and the development of  $\gamma/\gamma'$  interfacial dislocations has also been observed by TEM in Co-based superalloys, for example [41].

The lattice parameter misfit evolution during the 900 °C/260 MPa creep test of the sample with a cuboidal  $\gamma'$  microstructure and the sample subjected to the 800 °C/500 MPa creep test with an initially rafted  $\gamma'$  microstructure were similar, with a rapid increase in lattice parameter misfit over the first ~2% of creep strain, after which the lattice parameter misfit evolution was much slower, see Fig. 7. This is interpreted as the  $\gamma$  and  $\gamma'$  phases approaching unconstrained lattice parameter values, as coherency is lost. The lattice parameter misfit evolution of sample tested at 750 °C/875 MPa with a cuboidal  $\gamma'$  microstructure displayed slightly different kinetics to the other two creep tests. This was presumably due to different deformation mechanisms between the tests, in this case associated with the very high stress applied (875 MPa). Nonetheless, the lattice parameter misfit values were again very large and increased with creep strain.

The strength of precipitate-strengthened alloys is known to be related to the nature of the precipitate–matrix interface, and this interface was shown to be dramatically altered during creep deformation over a time frame of less than 10 h. Large lattice parameter misfit values between the  $\gamma$  and  $\gamma'$  phases may in fact be detrimental to the alloy. Prior to creep deformation, the  $\gamma$  and  $\gamma'$  phases are initially highly constrained by each other, keeping atomic coherency/semi-coherency. However, as creep strain accumulated, the constraint between phases appears to be quickly released, most probably by dislocations at the  $\gamma/\gamma'$  interfaces [41], with an associated loss of coherency. It is known from Ni-based superalloys that a loss of coherency can reduce the strength of the alloy by decreasing the coherency stresses in the neighborhood of the precipitates [40], and in particular to dramatically lower the low-cycle fatigue life [42]. The unconstrained lattice parameter misfit value approached during creep of the Ni-based superalloys was much lower [23] than that of the Co-based superalloys presented herein, and the Ni-based superalloys therefore maintain a more complete atomic registry between phases during creep deformation. This work highlights that large lattice parameter misfit values of the Co-based superalloys developed to date may be a cause of concern, and that a careful compositional design will need to take this parameter into account.

## 5. Conclusions

A ~50%  $\gamma'$  areal fraction Co-based superalloy single crystal was crept under tension at 940 °C/100 MPa/20 h, and the sample accumulated ~0.2% strain. This produced a ~25%  $\gamma'$  areal fraction of P-type rafts. Particle coalescence was observed in all <100> directions and was most dramatic in the direction of the tensile stress, suggesting that P-type rafts are not necessarily limited to a rod-like morphology exclusively aligned in a single direction.

Two creep experiments were performed with *in-situ* neutron diffraction at 900 °C/260 MPa, and at 750 °C/875 MPa, on samples with initially cuboidal  $\gamma'$  microstructures. A third *in-situ* experiment was performed at 800 °C/500 MPa, but with an initially rafted  $\gamma'$  microstructure.

The lattice parameter evolution of the  $\gamma$  and  $\gamma'$  phases indicated that a loss of interface coherency occurred between the phases for

all creep measurements, most likely associated with interface dislocations [41]. The lattice parameter misfit approached unconstrained values that were notably large compared to those of typical Ni-based superalloys. The loss of atomic registry at the precipitate-matrix interface has been shown to be of particular detriment to low-cycle fatigue strength of the Ni-based superalloys [42]. Thus, a notably lower level of atomic-registry at the  $\gamma/\gamma'$  interface (or a notably higher loss of coherency associated with the large difference in unconstrained lattice parameter values between phases) of the present Co-based superalloys during creep is of particular concern, and future compositional design should alter the alloy's compositions to decrease this mismatch in lattice parameters.

## Acknowledgements

The contributions of Stephen DiPietro at Exothermics Inc., New Hampshire; and John Koppes at Alcoa-Howmet Research Center, Michigan are acknowledged for material casting and heat-treatments. This work was performed under awards 70NANB14H012 from U.S. Department of Commerce, National Institute of Standards and Technology as part of the Center for Hierarchical Materials Design (ChiMad), and the European Union Seventh Framework Programme under the Marie Curie grant agreement No. 628643. The neutron scattering study at ORNLs Spallation Neutron Source was sponsored by the Scientific User Facilities Division, Office of Basic Energy Sciences, US Department of Energy. This work made use of the EPIC facility of the NUANCE Center at Northwestern University, supported by SHyNE Resource (NSF NNCI-1542205); the MRSEC program (NSF DMR-1121262) at the Materials Research Center; the Keck Foundation; and the State of Illinois, through the IIN.

## References

- [1] J. Sato, T. Omori, K. Oikawa, I. Ohnuma, R. Kainuma, K. Ishida, Cobalt-base high-temperature alloys, *Science* 312 (5770) (2006) 90–91.
- [2] A. Bauer, S. Neumeier, F. Pyczak, R.F. Singer, M. Göken, Creep properties of different  $\gamma'$ -strengthened Co-base superalloys, *Mater. Sci. Eng. A* 550 (2012) 333–341.
- [3] A. Bauer, S. Neumeier, F. Pyczak, M. Göken, Creep strength and microstructure of polycrystalline gamma-prime-strengthened cobalt-base superalloys, in: *Superalloys 2012: 12th International Symposium on Superalloys, 2012*, pp. 695–703.
- [4] F. Xue, H.J. Zhou, Q.Y. Shi, X.H. Chen, H. Chang, M.L. Wang, Q. Feng, Creep behavior in a  $\gamma'$  strengthened Co-Al-W-Ta-Ti single-crystal alloy at 1000 °C, *Scr. Mater.* 97 (2015) 37–40.
- [5] F. Xue, H.J. Zhou, Q. Feng, Improved high-temperature microstructural stability and creep property of novel Co-base single-crystal alloys containing Ta and Ti, *J.O.M.* 66 (12) (2014) 2486–2494.
- [6] F. Xue, H.J. Zhou, X.F. Ding, M.L. Wang, Q. Feng, Improved high temperature  $\gamma'$  stability of Co-Al-W-base alloys containing Ti and Ta, *Mater. Lett.* 112 (2013) 215–218.
- [7] K. Shinagawa, T. Omori, K. Oikawa, R. Kainuma, K. Ishida, Ductility enhancement by boron addition in Co-Al-W high-temperature alloys, *Scr. Mater.* 61 (2009) 612–615.
- [8] M.S. Titus, A. Suzuki, T.M. Pollock, Creep and directional coarsening in single crystals of new  $\gamma-\gamma'$  cobalt-base alloys, *Scr. Mater.* 66 (2012) 574–577.
- [9] K. Tanaka, M. Ooshima, N. Tsuno, A. Sato, H. Inui, Creep deformation of single crystals of new Co-Al-W-based alloys with fcc/L1<sub>2</sub> two-phase microstructures, *Phil. Mag.* 92 (32) (2012) 4011–4027.
- [10] M.S. Titus, Y.M. Eggeler, A. Suzuki, T.M. Pollock, Creep-induced planar defects in L1<sub>2</sub>-containing Co- and CoNi-base single-crystal superalloys, *Acta Mater.* 82 (2015) 530–539.
- [11] H.Y. Yan, V.A. Vorontsov, J. Coakley, N.G. Jones, H.J. Stone, D. Dye, Quaternary alloying effects and the prospects for a new generation of Co-base superalloys, in: *Superalloys 2012: 12th International Symposium on Superalloys, 2012*, pp. 705–714.
- [12] L. Klein, M.S. Killian, S. Virtanen, The effect of nickel and silicon addition on some oxidation properties of novel Co-based high temperature alloys, *Corros. Sci.* 69 (2013) 43–49.
- [13] M. Knop, P. Mulvey, F. Ismail, A. Radecka, K.M. Rahman, T.C. Lindley, B.A. Shollock, M.C. Hardy, M.P. Moody, T.L. Martin, P.A.J. Bagot, D. Dye, A new polycrystalline Co-Ni superalloy, *J.O.M.* 66 (12) (2014) 2495–2501.
- [14] S.K. Makineni, B. Nithin, K. Chattopadhyay, A new tungsten-free  $\gamma-\gamma'$  Co-Al-Mo-Nb-based superalloy, *Scr. Mater.* 98 (2015) 36–39.
- [15] S.K. Makineni, B. Nithin, K. Chattopadhyay, Synthesis of a new tungsten-free  $\gamma-\gamma'$  cobalt-based superalloy by tuning alloying additions, *Acta Mater.* 85 (2015) 85–94.
- [16] H.Y. Yan, J. Coakley, V.A. Vorontsov, N.G. Jones, H.J. Stone, Dye alloying and the micromechanics of Co-Al-W-X quaternary alloys, *Mater. Sci. Eng. A* 613 (2014) 201–208.
- [17] F. Pyczak, A. Bauer, M. Göken, U. Lorenz, S. Neumeier, M. Oehring, J. Paul, N. Schell, A. Schreyer, A. Stark, F. Symanzik, The effect of tungsten content on the properties of L1<sub>2</sub>-hardened Co-Al-W alloys, *J. Alloys Compd.* 635 (2015) 110–115.
- [18] P.J. Bocchini, E.A. Lass, K.W. Moon, M.E. Williams, C.E. Campbell, U.R. Kattner, D.C. Dunand, D.N. Seidman, Atom-probe tomographic study of  $\gamma/\gamma'$  interfaces and compositions in an aged Co-Al-W superalloy, *Scr. Mater.* 68 (8) (2013) 563–566.
- [19] Q. Liu, J. Coakley, D.N. Seidman, D.C. Dunand, Precipitate evolution and creep behavior of a W-free Co-based superalloy, *Metall. Mater. Trans. A* 47 (2016) 6090–6096.
- [20] J. Coakley, E.A. Lass, D. Ma, M. Frost, D.N. Seidman, D.C. Dunand, H.J. Stone, Rafting and elastoplastic deformation of superalloys studied by neutron diffraction, *Scr. Mater.* 134 (2017) 110–114.
- [21] F.R.N. Nabarro, Rafting in superalloys, *Metall. Mater. Trans. A* 27 (3) (1996) 513–530.
- [22] D. Dye, J. Coakley, V.A. Vorontsov, H.J. Stone, R.B. Rogge, Elastic moduli and load partitioning in a single-crystal nickel superalloy, *Scr. Mater.* 61 (2) (2009) 109–112.
- [23] J. Coakley, D. Ma, M. Frost, D. Dye, D.N. Seidman, D.C. Dunand, H.J. Stone, Lattice strain evolution and load partitioning during creep of a Ni-based superalloy single crystal with rafted  $\gamma'$  microstructure, *Acta Mater.* 135 (2017) 77–87.
- [24] R.A. Ricks, A.J. Porter, R.C. Ecob, The growth of  $\gamma'$  precipitates in nickel-base superalloys, *Acta Metall.* 31 (1983) 43–53.
- [25] R.F. Decker, J.R. Mihalisin, Coherency strains in  $\gamma'$  hardened nickel alloys, *Trans. Am. Soc. Metals Q.* 62 (1969) 481–489.
- [26] N. Matan, D.C. Cox, C.M.F. Rae, R.C. Reed, On the kinetics of rafting in CMSX-4 superalloy single crystals, *Acta Mater.* 47 (7) (1999) 2031–2045. Z. Sun, et al, Load partitioning between the bcc-iron matrix and NiAl-type precipitates in a ferritic alloy on multiple length scales, *Sci. Rep.* 6 23137, doi:10.1038/srep23137 (2016).
- [27] G. Song, Z. Sun, L. Li, B. Clausen, S.Y. Zhang, Y. Gao, P.K. Liaw, Load partitioning between the bcc-iron matrix and NiAl-type precipitates in a ferritic alloy on multiple length scales, *Sci. Rep.* 6 (2016) 23137.
- [28] Z. Sun, G. Song, T.A. Sisneros, B. Clausen, C. Pu, L. Li, Y. Gao, P.K. Liaw, High temperature deformation mechanism in hierarchical and single precipitate strengthened ferritic alloys by in situ neutron diffraction studies, *Sci. Rep.* 7 (2017) 45965.
- [29] T.M. Pollock, A.S. Argon, Directional coarsening in nickel-base single crystals with high volume fractions of coherent precipitates, *Acta Metall. Mater.* 42 (6) (1994) 1859–1874.
- [30] H. Mughrabi, The importance of sign and magnitude of  $\gamma/\gamma'$  lattice misfit in superalloys-with special reference to the new  $\gamma'$ -hardened cobalt-base superalloys, *Acta Mater.* 81 (2014) 21–29.
- [31] J.K. Tien, R.P. Gamble, Effects of stress coarsening on coherent particle strengthening, *Metall. Trans.* 3 (8) (1972) 2157–2162.
- [32] J. Coakley, R.C. Reed, J.L.W. Warwick, K.M. Rahman, D. Dye, Lattice strain evolution during creep in single-crystal superalloys, *Acta Mater.* 60 (2012) 2729–2738.
- [33] K. An, H.D. Skorpenske, A.D. Stoica, D. Ma, X.L. Wang, E. Cakmak, First in situ lattice strains measurements under load at VULCAN, *Metall. Mater. Trans. A* 42 (1) (2011) 95–99.
- [34] H.J. Stone, T.M. Holden, R.C. Reed, On the generation of microstrains during the plastic deformation of Waspaloy, *Acta Mater.* 47 (17) (1999) 4435–4448.
- [35] J. Coakley, D. Dye, Lattice strain evolution in a high volume fraction polycrystal nickel superalloy, *Scr. Mater.* 67 (5) (2012) 435–438.
- [36] A.J. Ardell, R.B. Nicholson, On the modulated structure of aged Ni-Al alloys: with an Appendix on the elastic interaction between inclusions by J. D. Eshelby, *Acta Metall.* 14 (1966) 1295–1309.
- [37] H. Ohtani, M. Yamano, M. Hasebe, Thermodynamic analysis of the Co-Al-C and Ni-Al-C systems by incorporating ab initio energetic calculations into the CALPHAD approach, *Calphad* 28 (2) (2004) 177–190.
- [38] J. Miettinen, Thermodynamic description of the Cu-Al-Ni system at the Cu-Ni side, *Calphad* 29 (1) (2005) 40–48.
- [39] H.J. Stone, T.M. Holden, R.C. Reed, Determination of the plane specific elastic constants of Waspaloy using neutron diffraction, *Scr. Mater.* 40 (3) (1999) 353–358.
- [40] A.K. Singh, N. Louat, K. Sadananda, Dislocation network formation and coherency loss around gamma-prime precipitates in a nickel-base superalloy, *Metall. Trans. A* 19 (1988) 2965–2973.
- [41] F. Pyczak, A. Bauer, M. Göken, S. Neumeier, U. Lorenz, M. Oehring, N. Schell, A. Schreyer, A. Stark, F. Symanzik, Plastic deformation mechanisms in a crept L1<sub>2</sub> hardened Co-base superalloy, *Mater. Sci. Eng. A* 571 (2015) 13–18.
- [42] A. Epishin, T. Link, H. Klingelhöffer, P.D. Portella, Creep damage of single-crystal nickel base superalloys: mechanisms and effect on low cycle fatigue, *Mater. High Temp.* 27 (1) (2010) 5359.